ChemSusChem

Research Article
doi.org/10.1002/cssc.202300631

Chemistry Europe
European Chemical Societies Publishing

www.chemsuschem.org

Special Collection

Stabilizing Decavanadate Cluster as Electrode Material in Sodium and Lithium-ion Batteries

Meena Ghosh,*[a] Dieter Sorsche,[a] Rezwana Binte Ahmed,[a] and Montaha Anjass*[a, b, c]

Decavanadate ($[V_{10}O_{28}]^{6-}$, $\{V_{10}\}$) clusters are a potential electrode material for lithium and post-lithium batteries; however, their low stability due to the solubility in liquid organic electrolytes has been challenging. These molecular clusters are also prone to transform into solid-state oxides at a moderate temperature needed in the typical electrode fabrication process. Hence, controlling the solubility and improving the thermal stability of compounds are essential to make them more viable options for use as battery electrodes. This study shows a crystal engineering approach to stabilize the cluster with organic guanidinium (Gdm^+) cation through the hydrogen-bonding interactions between the amino groups of the cation and the anion. The comparison of solubility and thermal stability of the Gdm$\{V_{10}\}$ with another cluster bearing tetrabutylammonium (Tba^+) cation reveals the better stability of cation-anion assembly in the former than the latter. As a result, the Gdm$\{V_{10}\}$ delivers better rate capability and cycling stability than Tba$\{V_{10}\}$ when tested as anode material in a half-cell configuration of a sodium-ion battery. Finally, the performance of the Gdm$\{V_{10}\}$ anode is also investigated in a lithium-ion battery full cell with $LiFePO_4$ cathode.

Introduction

Polyoxometalates (POMs), the anionic oxo clusters of high-valent early transition metals (often V, Mo, and W), are emerging materials with redox properties relevant to electrochemical energy storage and conversion devices.[1] They form large and closed three-dimensional discrete molecular structures through the self-assembly of the oxometallate precursors during the solution-phase synthesis.[2] As molecular analogs, POM combines the merits of metal oxides in terms of physicochemical and functional properties with the scope of molecular design flexibility. Besides, the ease of modulating the structure and properties of POMs at the molecular level by introducing different heteroatom, ligands, addenda atoms, counterions, etc., encouraged investigating their redox properties for broad applications, including lithium and post-lithium batteries.[1a,3] Among other POMs, the polyoxovanadates (POVs) family is intriguing as battery electrode materials because of their rich redox activity (multiple accessible oxidation states, mainly V^V, V^{IV}, and more rarely V^{III}), which in principle enables the storage of multiple electrons per V atom. In addition, they offer lower molecular weight than other POM families, which allows higher gravimetric energy densities.[3] Furthermore, POVs feature more structural diversity and ease of tuning the redox activity. The decavanadate $M_6[V_{10}O_{28}]\cdot xH_2O$ (M: counter cation; x = 9–16) cluster ($\{V_{10}\}$) is a common POV prototype studied as battery electrodes.[4] They are the simplest clusters in the POV family and are easy to synthesize on a large scale under aqueous conditions. However, the as-synthesized crystal structure often contains many water molecules (e.g., $Li_6[V_{10}O_{28}]\cdot 16H_2O$),[5] which could lead to gas evolution (O_2 and H_2) under operating conditions of nonaqueous batteries and damage the battery performance. Therefore, removing the lattice water through thermal treatment at a high temperature (200 to 600 °C) is often followed in most studies.[5–6] In contrast, our recent work demonstrated that these clusters are susceptible to structural rearrangement upon thermal dehydration and form vanadium oxide species (e.g., LiV_3O_8 and $LiVO_3$) even at a moderate temperature of 120 °C.[7] Nevertheless, the low thermal stability of $\{V_{10}\}$ hinders evaluating its electrochemical properties as the molecular electrode component. These limitations can be addressed through molecular engineering using appropriate counter-cations and template atoms to stabilize the cluster. For example, another work from our group demonstrated that the molecular engineering approach introducing organic dimethylammonium (DMA^+) counterion improves the cluster's thermal stability compared to the Li^+ counterpart.[8]

[a] Dr. M. Ghosh, Dr. D. Sorsche, R. Binte Ahmed, Dr. M. Anjass
Institute of Inorganic Chemistry I
Ulm University
Albert-Einstein-Allee 11, D-89081 Ulm (Germany)
E-mail: meena.ghosh1992@gmail.com
montaha.anjass@uni-ulm.de
Homepage: www.anjassgroup.net

[b] Dr. M. Anjass
Departement of Chemistry
University of Sharjah
Sharjah-27272, Sharjah Sharjah (United Arab Emirates)

[c] Dr. M. Anjass
Helmholtz Institute Ulm (HIU)
Helmholtzstraße 11, D-89081 Ulm (Germany)

Supporting information for this article is available on the WWW under https://doi.org/10.1002/cssc.202300631

Special Collection This publication is part of a joint Special Collection of ChemSusChem, Batteries & Supercaps, and Energy Technology including invited contributions focusing on the "International Conference on Sodium Batteries (ICNaB)". Please visit chemsuschem.org/collections to view all contributions.

Besides, the $\{V_{10}\}$ cluster stabilized with DMA^+ cation contains a significantly lower number of crystalline water molecules that induce detrimental effects when considering its application in nonaqueous batteries. However, such studies exploring the effect of organic cations on the structural and electrochemical properties of the $\{V_{10}\}$ cluster or other POMs are rare.[4c,9]

Apart from thermal stability, investigating the solubility of $\{V_{10}\}$ clusters in connection with counterions in the aqueous and organic medium is equally essential for making them suitable for a particular application. POV clusters are soluble in a variety of solvents due to the high negative charge of POV anions, making them a suitable choice as electrolyte components in redox flow batteries.[10] However, when considering the application as battery electrode materials, the solubility trait is undesirable as it causes the active material leaching into the electrolyte and hampers the battery performance. In general, the solution stability of the POV-cation assembly relies on the complex interplay between the ion-pair strength through electrostatic, hydrogen bond interactions, etc., and the solvation property of the cation.[11] If the cation carries a strongly bound solvation shell, the solvent molecules inhibit the direct cation-anion interaction, promoting the solubility of the POV salt. Likewise, the weak ion-pair interaction also inhibits the direct precipitation of cation-POV ($\{V_{10}\}$ as an example) assembly in the aqueous reaction medium. In this case, recovering the final products from the aqueous solution often requires an additional step, e.g., evaporating the water at a low temperature, precipitation using a poor solvent, etc.[4c,8] Therefore, pairing $\{V_{10}\}$ with a suitable counterion that can simultaneously impart strong ion-pair interaction and improved thermal stability is an interesting approach to achieving their full potential as battery electrode materials.

Here, we investigated the stabilization of the $\{V_{10}\}$ cluster with the organic guanidinium (Gdm^+) ion for its application as anode material in sodium and lithium-ion batteries. The Gdm^+ ion is a well-known protein-denaturing agent (ability to precipitate protein in water) and most weakly hydrated cations with almost no distinct hydration shell.[12] The Gdm^+ ion can strongly interact with the functional groups in protein chains in aqueous medium, leading to the protein's precipitation. Inspired by this exceptional hydration property, we anticipated that Gdm^+ could also effectively stabilize $\{V_{10}\}$ anion through direct ion-pair interaction. The study explored the effect of Gdm^+ cation on the cluster's crystal structure, thermal stability, solubility, and electrochemical performance. The advantage of the Gdm^+ ion was evident from the poor solubility of the Gdm $\{V_{10}\}$ compound in the aqueous and organic medium, resulting in better electrochemical performance compared to another $\{V_{10}\}$ cluster bearing tetrabutyl ammonium (Tba^+) ion. The Tba^+ ion was selected for comparison as both cations can directly precipitate the $\{V_{10}\}$ cluster in the aqueous reaction medium, which makes the synthesis process simple. This work shows a straightforward route of crystal engineering to stabilize the $\{V_{10}\}$ cluster for electrode material development that can be also extended to other POMs.

Results and Discussion

Physical characterization

The schematic of the wet-chemical synthesis of Gdm$\{V_{10}\}$ and its crystal structure are presented in Figure 1a. The Gdm$\{V_{10}\}$ was synthesized from the aqueous solution of commercial V_2O_5 precursor dissolved using 6 M NaOH. The solution color changed from colorless to orange (at pH = 4.5) with the addition of 4 M HCl, indicating the formation of decavanadate ($[V_{10}O_{28}]^{6-}$, $\{V_{10}\}$) species. Adding an aqueous solution of guanidinium (Gdm^+) ion resulted in the precipitation of the bright-orange product (Gdm$\{V_{10}\}$). Similarly, the decavanadate cluster with tetrabutyl ammonium (Tba^+) ion was also prepared for comparison. In general, the aqueous-phase synthesis of $\{V_{10}\}$ compounds requires adding a less polar solvent (e.g., ethanol) in the final step to obtain precipitation of the product. This step is necessary because the high charge density of $\{V_{10}\}$ makes it soluble in a strongly polar solvent such as water and arrests the precipitation in the aqueous reaction mixture. Adding a large volume of ethanol reduces the solubility of $\{V_{10}\}$ by adjusting the polarity of the aqueous solution. Interestingly, adding Gdm^+ or Tba^+ could immediately isolate the final products from solutions, thereby eliminating the requirement for a second solvent for product recovery. This observation suggests that both cations can impart optimal ion-pair interaction with the $\{V_{10}\}$ cluster to stabilize the cation-$\{V_{10}\}$ assembly in the respective aqueous reaction mixtures. Despite the stability of the Gdm$\{V_{10}\}$ and Tba$\{V_{10}\}$ complexes in the aqueous medium, they exhibited different behavior when introduced in the organic polar solvents (e.g., acetonitrile, Figure 1c). The Gdm

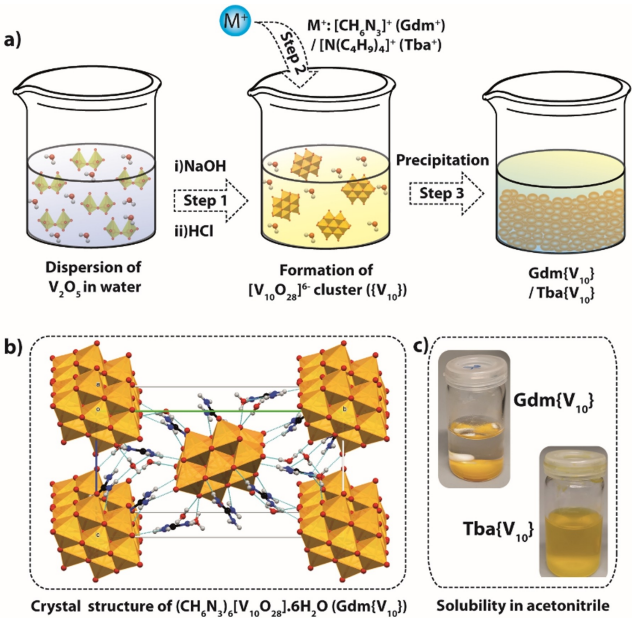

Figure 1. (a) Scheme representing the reaction steps involved in the synthesis of the Gdm$\{V_{10}\}$ and Tba$\{V_{10}\}$; (b) the mixed stick-and-ball/polyhedral representation of Gdm$\{V_{10}\}$ crystal structure in the crystallographic bc-plane; Colour scheme: V (orange); O (red), C (clack), N (blue), H (grey). (c) solubility of as-synthesized Gdm$\{V_{10}\}$ and Tba$\{V_{10}\}$ in acetonitrile.

$\{V_{10}\}$ compound is insoluble in various organic solvents with a wide range of polarity (e.g., acetonitrile, dimethyl formamide, N-methyl-2-pyrrolidone, dimethyl sulfoxide, diethyl carbonate, etc.). In contrast, adding Tba$\{V_{10}\}$ to these solvents resulted in an immediate color change to yellow, indicating the dissolution of the compound (Figure 1c).

The insoluble nature of the Gdm$\{V_{10}\}$ arises from the strong association of the ion pair through electrostatic attraction and the formation of multiple hydrogen bonds. The three amine groups in Gdm^+ can engage in an extended hydrogen bonding interaction with the anion cluster, strengthening the Gdm$\{V_{10}\}$ ion-pair assembly. Although Tba^+ also extends similar interactions, the compound's solubility in high-polarity solvents, e.g., acetonitrile, indicates the strength of ion-pair interactions in the Tba$\{V_{10}\}$ assembly is weaker. The weaker cation-anion interaction in Tba$\{V_{10}\}$ is presumably due to the large size and low charge density of Tba^+, which hinder its ability to strongly interact with the negatively charged $\{V_{10}\}$ cluster through electrostatic interaction. Besides, unlike Gdm^+, the absence of the acidic proton in Tba^+ also lead to weak hydrogen bond interaction in Tba$\{V_{10}\}$ clusters. Consequently, the ion-pair assembly in Tba$\{V_{10}\}$ gets easily disrupted in highly polar organic solvents, triggering the dissolution of the compound.

For the single-crystal X-ray diffraction (SC-XRD) characterization, the single crystals of Gdm$\{V_{10}\}$ were obtained by dissolving the material in hot water (at 65 °C) followed by slow diffusion of ethanol into the solution. The SC-XRD data gave the chemical formula $(CN_3H_6)_6[V_{10}O_{28}]\cdot 6H_2O$ of the Gdm$\{V_{10}\}$ crystallizes in the $P2_1/n$ space group with cell axes a = 9.20 Å, b = 21.91 Å and c = 11.15 Å, and angles $\alpha = 90$, $\gamma = 90$ and $\beta = 103.9°$, V = 2183.42 Å^3 (for crystallographic details see SI, Table S1). The crystal structure of Gdm$\{V_{10}\}$ (Figure 1b) confirms the existence of $\{V_{10}\}$ clusters, where each $\{V_{10}\}$ cluster is connected to six guanidinium cations to balance the negative charge of each decavanadate anion. As shown in Figure S1, sixteen oxygen atoms from the $\{V_{10}\}$ cluster form hydrogen bonds with $-NH_2$ groups of Gdm^+ counterion. The crystal structure also contains six water molecules sharing hydrogen bonding with the $\{V_{10}\}$ cluster and Gdm^+ cation. The crystal structure and composition of Gdm$\{V_{10}\}$ match the previous report.[13] The powder XRD (PXRD) profile of bulk Gdm$\{V_{10}\}$ also matches the simulated pattern obtained from scXRD data (Figure 2a), confirming the phase purity of the as-synthesized compound. Notably, the choice of charge-balancing cation influences the lattice array, composition, and the number of water molecules in the crystal structure of $\{V_{10}\}$ compounds. For instance, the number of water molecules in Gdm$\{V_{10}\}$ is significantly less than other $\{V_{10}\}$ clusters with Li^+ or Na^+ counterion ($Li_6[V_{10}O_{28}]\cdot 16H_2O$).[7] The difference is caused by the substantial hydration property of these alkali ions, whereas the Gdm^+ ion has a poor hydration feature. On the other hand, using Tba^+ counterion is known to crystallize into $((C_4H_5)_4N)_3[H_3V_{10}O_{28}]$ devoid of crystalline water molecules.[14] The absence of water molecules in the crystal structure of Tba$\{V_{10}\}$ could be attributed to the hydrophobic character of the butyl chains in the Tba^+ cation.

The thermal stability of the compounds was analyzed with thermogravimetric analysis (TGA) in an air atmosphere. In the TGA profile of Gdm$\{V_{10}\}$ (Figure 2b), the initial weight loss of 2.1 wt.% below 100 °C corresponds to the removal of water molecules from the compound (approximately two water molecules), followed by a plateau up to 220 °C. This plateau

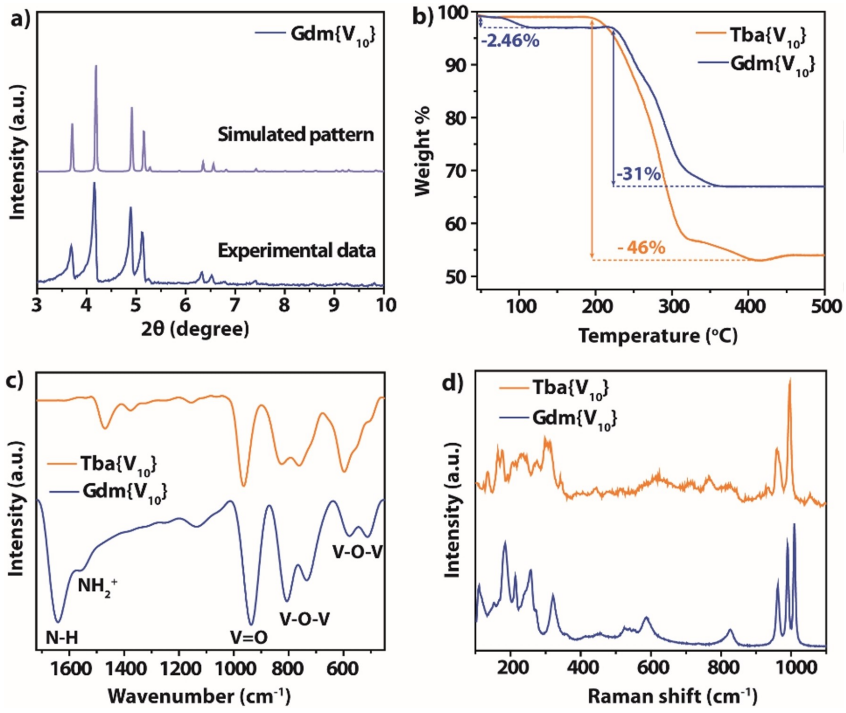

Figure 2. (a) Experimental and simulated powder XRD pattern of the Gdm$\{V_{10}\}$; (b) TGA, (c) FTIR, and (d) Raman profiles of the Gdm$\{V_{10}\}$ and Tba$\{V_{10}\}$ clusters.

feature is distinct from the sloped behavior observed for $Na_6[V_{10}O_{28}]\cdot 16H_2O$ and $Li_6[V_{10}O_{28}]\ 16H_2O$ in a similar temperature range.[1a,8] As mentioned in our previous works, the slopy feature in the low-temperature range of the TGA data of these compounds signifies the transformation of the molecular cluster into vanadium oxide species upon thermal dehydration.[8] In other words, the plateau in Gdm{V_{10}} indicates better thermal stability of the cluster despite the partial removal of crystalline water. Further, an increase in temperature beyond 220 °C leads to a sharp weight loss of ca. 31% caused by the loss of the six guanidine moieties and the remaining four water molecules. The TGA profile of Tba{V_{10}} (Figure 2b) also exhibits a plateau followed by a sharp weight loss of ca. 46% above 190 °C temperature, indicating the loss of three Tba^+ molecules. This trend aligns with previous literature, where Tba^+ molecules in other polyoxometalates decompose at similar temperatures.[15] Notably, no initial weight loss below 100 °C is observed in the case of Tba{V_{10}}, further indicating the absence of crystalline water molecules in the compound. It can be noticed that the mass loss starts at a slightly lower temperature in Tba{V_{10}} (~190 °C) than that in Gdm{V_{10}} (~220 °C), which implies stronger interaction between Gdm^+ ion and {V_{10}} cluster than ammonium cation.[16] However, the thermal stability of both samples is much better than Li or Na-based {V_{10}} clusters. Also, no apparent decomposition of the samples with Gdm^+ and Tba^+ ions up to 200 °C ensures that both compounds have sufficient thermal stability to retain their molecular structure during the electrode preparation steps (e.g., electrodes prepared from NMP-based slurry require drying at 80–120 °C under vacuum). Considering the desired thermal stability of Gdm{V_{10}} and Tba{V_{10}}, these two materials were taken forward for further analysis and electrochemical performance evaluation.

The structure and various metal-oxo bonds present in the as-synthesized Gdm{V_{10}} cluster were analyzed by FTIR and Raman spectroscopy. In the FTIR spectra (Figure 2c), the intense peak at 933 cm^{-1} corresponds to the characteristic terminal V=O bonds, whereas the bridging V–O–V bonds appear at 508, 580, 734, and 810 cm^{-1}.[17] The peaks at 1560 and 1639 cm^{-1} originate from the C=N bond of the guanidine moiety.[18] The fingerprint region of the FTIR spectra (1000 to 450 cm^{-1}) for Tba{V_{10}} more or less overlaps with that of the Gdm{V_{10}}, suggesting that the change in counterion has not influenced the metal-oxo bonds in the decavanadate cluster. In the Raman spectra (Figure 2d), the peaks corresponding to V=O and V–O–V bonds in Gdm{V_{10}} and Tba{V_{10}} also comply with the results obtained from FTIR analysis.

Later, the FTIR and XRD analysis of the samples heated at higher temperatures (>120 °C) was also performed to investigate the thermal stability of the Gdm{V_{10}} cluster. Figure S2a shows that the Gdm{V_{10}}-150 doesn't show a noticeable change in FTIR spectra. However, after heating to 200 °C, the characteristic peaks for V=O and V–O–V bonds show significantly reduced intensity or disappear, which indicates a substantial structural rearrangement in the cluster. This observation is in line with the corresponding TGA profile displaying a sharp weight loss at 220 °C. The XRD profiles in Figure S2b also show the change in the crystal structure of Gdm{V_{10}} as a function of temperature. In line with the FTIR results, after heating up to 200 °C the diffraction peaks of Gdm{V_{10}} appeared significantly different than the original sample, indicating the formation of a new crystal phase. The change in sample color from orange to brown (Figure S2c) upon heating at 200 °C also gives a visual indication of the deformation of the crystal structure. Apart from thermal stability, the structural stability of the Gdm{V_{10}} cluster at ambient conditions is further confirmed. The FTIR and XRD data in Figure S2d and e display that the material doesn't show noticeable decomposition when stored in the air for several months, suggesting its high stability toward moisture and air.

As observed from the SEM image (Figure 3a), the Gdm{V_{10}} sample forms rod-shaped crystals. On the other hand, the Tba{V_{10}} (Figure 3b) possesses large aggregates of small and irregular-shaped particles. The apparent difference in the morphology of Gdm{V_{10}} and Tba{V_{10}} underlines the influence of the charge-balancing cation on the crystal growth pattern. The elements' chemical composition and oxidation states were probed with XPS measurements. The XPS survey spectra of Gdm{V_{10}} and Tba{V_{10}} samples (Figures S3a and b, respectively) display C, N, O, and V presence in both samples. In Figure 3c, the sharp peak at 530.0 eV in the O1s region is assigned to the V–O bond in the {V_{10}} cluster in Gdm{V_{10}}. The XPS analysis of V2p (Figure 3c) shows a sharp signal in the $V2p_{3/2}$ region at binding energies of ~517 eV (assigned to V^V),[19] indicating that the vanadium centers in the cluster are in the V^V oxidation state. The XPS data of the Tba{V_{10}} sample also shows the O1s and V2p signals at 529.8 and 516.8 eV, respectively (Figure S3c). The N1s spectra for Gdm{V_{10}} (Figure 3d) and Tba{V_{10}} (Figure S3d) display a single peak at the binding energy of 399.9 and 401.7 eV, respectively.

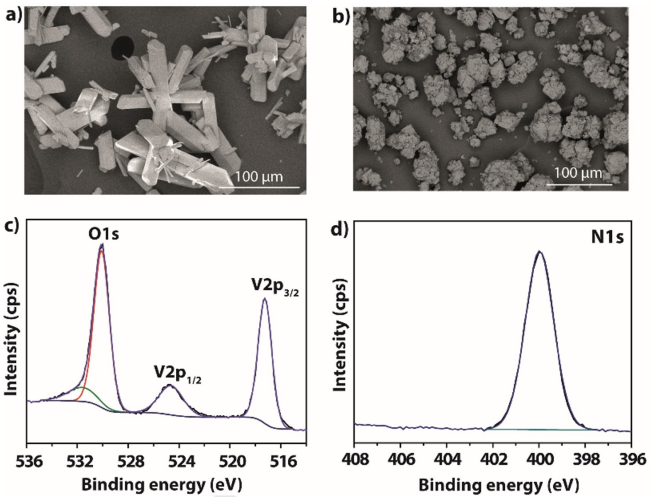

Figure 3. SEM images of (a) Gdm{V_{10}} and (b) Tba{V_{10}}; deconvoluted XPS (c) V2p and (d) N1s of the Gdm{V_{10}} compound.

Electrochemical characterization in sodium-Ion battery half-cell configuration

The electrochemical performance of the Gdm{V_{10}} and Tba{V_{10}} electrodes (see experimental section details of the electrode preparation steps in SI) as anode material for sodium-ion batteries (SIBs) was compared in the half-cell configuration. The galvanostatic charge-discharge (GCD) of the Na||Gdm{V_{10}} (Figure S4a) from the open circuit potential (OCP, 2.5 V vs. Na^+/Na) at 0.02 A g^{-1} current rate shows a small plateau at 1.5 V vs. Na^+/Na followed by a sloped feature in the low potential region. The specific discharge capacity obtained from the first discharge cycle is 328 mAh g^{-1}. However, the cell could retrieve only 95 mAh g^{-1} capacity in the reverse charge cycle, corresponding to a low initial Coulombic efficiency (CE) of 28% in the first cycle. Although the low CE value is not desirable while considering the aptness of this material as a SIB anode, this drawback can be overcome by adopting presodiation strategies.[20] In the following cycles, the electrode exhibits a sloped GCD profile, and the charge storage capacity gradually increases with an improvement in CE. As a result, the reversible discharge capacity of the electrode at 50th, 100th, and 150th cycles are 133, 209, and 225 mAh g^{-1} (Figure 4a). The difference observed in the first discharge profile is due to the partial decomposition of the electrolyte in the first cycle with the subsequent formation of solid electrolyte interphase, as observed in several other reports.[21] A similar feature with a low first-cycle CE value is also evidenced in Na||Tba{V_{10}} cell (Figure S4b). The cell delivers a specific capacity of 396 mAh g^{-1} when discharged from OCP of 2.7 V to 0.005 V vs. Na^+/Na (1st discharge) and 226 mAh g^{-1} in the 2nd discharge. The discharge capacity of the Tba{V_{10}} electrode at 50th, 100th, and 150th cycles are 83, 66, and 59 mAh g^{-1} (Figure S4c).

Figure 4b shows the rate capability performance of Gdm{V_{10}} and Tba{V_{10}} anodes. Gdm{V_{10}} delivers discharge capacity of 135, 86, 67, 49, and 41 mAh g^{-1} at current densities of 0.02, 0.05, 0.1, 0.25, and 0.5 A g^{-1} respectively. As the current is further restored to 0.02 A g^{-1}, the material can still recover

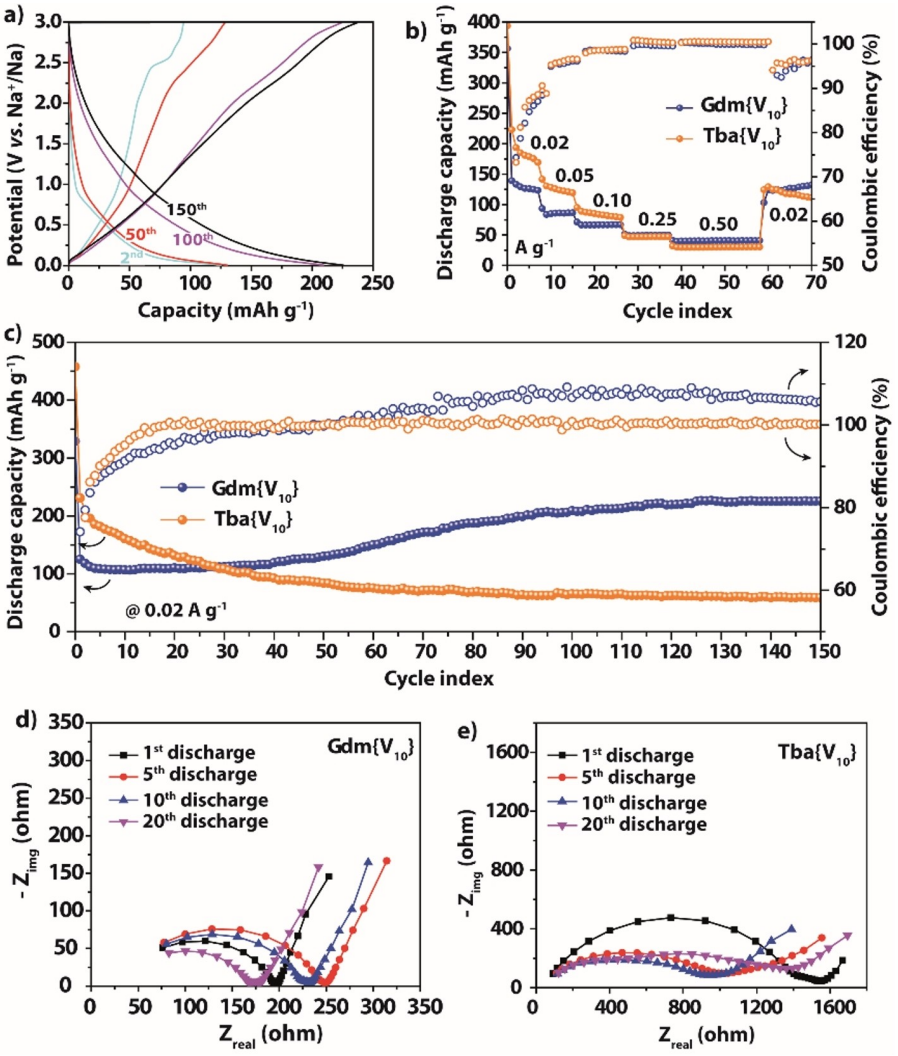

Figure 4. Electrochemical performance of Na||Gdm{V_{10}} and Na||Tba{V_{10}} cells (a) selected cycles of galvanostatic cycling of Na||Gdm{V_{10}} cell recorded at 0.02 A g^{-1} current rate and potential range of 0.005 to 3.0 V vs. Na^+/Na; (b) rate capability (c) cycling stability performance (at 0.02 A g^{-1}) of the Na||Gdm{V_{10}} and Na||Tba{V_{10}} cells; Nyquist profiles of (d) Na||Gdm{V_{10}} and (e) Na||Tba{V_{10}} recorded after various cycles.

130 mAh g^{-1} even after 70 cycles, indicating good rate performance of the Gdm{V_{10}} electrode. The rate performance of the cell appears to be more or less consistent regardless of whether the cell was cycled prior to the rate test (Figure S4d). The specific capacity of the Tba{V_{10}} (222 mAh g^{-1} at 0.02 A g^{-1}) is relatively higher than that of Gdm{V_{10}} (Figure 4b), although both samples show an irreversible capacity loss in the first cycle. Unlike Gdm{V_{10}} possessing micrometer-length crystals, the Tba{V_{10}} has a much smaller particle size, which enhances the active material utilization in the redox reactions, leading to a higher charge storage capacity. The discharge capacity values for the Tba{V_{10}} electrode at different current densities of 0.02, 0.05, 0.1, 0.25, and 0.5 A g^{-1} are 222, 126, 83, 47, and 30 mAh g^{-1}, respectively (Figure 4b). Nevertheless, the cell could recover only 128 mAh g^{-1} capacity when the current rate is reverted to 0.02 A g^{-1}, a value much lower than the initial capacity (222 mAh g^{-1}) obtained at the same current rate.

The cyclic voltammetry (CV) profiles of both cells recorded at various scan rates are presented in Figures S5a–d. In both cases, the CV curve in the 1st cathodic scan appears different than in the following cycles (Figure S5a and b). The higher current traced in the 1st scan is in line with the GCD data of the respective samples, as explained in Figure S5a and b. The CV cycles of Na||Gdm{V_{10}} display a nearly overlapping feature and increase in the current response with an increase in the scan rates (Figure S5c), indicating good electrochemical reversibility of the Gdm{V_{10}} electrode. The higher peak current traced in the low potential region (0.87 to 0.02 V vs. Na^+/Na) of CV scans suggests the suitability of the compound as an anode material for SIBs. Similarly, the CV profiles of Na||Tba{V_{10}} cell (Figure S5d) also trace reversible redox features at the low potential region, although with relatively higher reduction peak current (0.69 A g^{-1}) than Na||Gdm{V_{10}} cell (0.56 A g^{-1}). The higher current response in the Tba{V_{10}} electrode is also consistent with the higher capacity obtained from the galvanostatic charge-discharge analysis of the cell.

Later, the long-term cycling stability of Gdm{V_{10}} and Tba{V_{10}} anodes was tested at a current density of 0.02 A g^{-1}. As shown in Figure 4c, Gdm{V_{10}} cell shows a drop in the capacity value from 325 mAh g^{-1} in the 1st discharge to 120 mAh g^{-1} in the 2nd cycle. However, such capacity loss from the electrochemical irreversibility is significant only in the 1st cycle and diminishes in the following cycles. Subsequently, the CE value of the cell also improves in the following cycles. After a few initial cycles, the reversible capacity gradually increases, and the electrode could deliver 224 mAh g^{-1} discharge capacity after 150 cycles. It is observed that the long-term cycling resulted in a slightly higher charge capacity than discharge capacity (Figure 4a) leading to a CE value above 100%. This feature could result from the irreversible side reactions on the Na metal counter electrode during cycling.[22] The increase in discharge capacity suggests that the electrode material undergoes a slow yet continuous electrochemical activation during progressive cycling. A similar electrochemical signature showing increased capacity with cycling has been observed for other electrode materials reported earlier.[23] The Gdm{V_{10}} electrode also displayed good cycling stability at a higher current rate of 0.1 A g^{-1}, showing 83% capacity retention over 500 cycles (Figure S6). On the other hand, the Tba{V_{10}} electrode (Figure 4c) delivers an initial capacity of 393 and 190 mAh g^{-1} (in the 1st and 2nd discharge cycles, respectively) but suffers from a steady performance decay during the cycling process. As a result, the cell could show only 65 mAh g^{-1} capacity after 100 cycles, indicating inferior durability of the Tba{V_{10}} electrode compared to Gdm{V_{10}}.

To validate the observed trend in the cycling stability of Gdm{V_{10}} and Tba{V_{10}}, the electrochemical impedance spectra (EIS) of the cells recorded after the 1st, 5th, 10th, and 20th discharge are compared. The Nyquist plots display a higher charge transfer resistance (R_{ct}) of the Tba{V_{10}} (Figure 4e) cell than that of Gdm{V_{10}} (Figure 4d). Besides, the R_{ct} value of the Gdm{V_{10}} cell gradually decreases with cycling (the values recorded after the 5, 10, and 20th cycles are 200, 175, and 125 Ω, respectively), which is indicative of a more facile electrochemical process. The improvement in Gdm{V_{10}} cell's resistance correlates well with its capacity enhancement during the cycling stability test. However, further studies are necessary to reveal the origin of capacity increase by investigating the change in particle size, amorphization, etc., of the active material due to cycling. The Nyquist plots for the Tba{V_{10}} cell exhibit R_{ct} values of 1000 Ω, 900 Ω, and 1255 Ω after 5, 10, and 20 GCD cycles, respectively. The overall higher impedance of the Tba{V_{10}} cell substantiates its inferior cycling performance.

The considerable difference observed in the cycling and impedance performance is ascribed to the different physical properties of these systems despite possessing identical redox centers in the {V_{10}} clusters. Whereas the Gdm{V_{10}} material remains insoluble in the liquid organic electrolyte ($NaPF_6$ in tetraglyme) used in the SIB half cells, the significant dissolution of the Tba{V_{10}} compound is evident (Figure S7a) from the color change of the electrolyte to yellow. As a result, a yellow tinge on the glass fiber separator was also observed while assembling the cell with Tba{V_{10}} material (Figure S7b). The dissolution of the Tba{V_{10}} in the electrolyte causes active material loss from the electrode, leading to capacity fading during cycling. Nevertheless, the dissolved materials can diffuse through the porous separator and poison the counter electrode, which impedes the overall electrochemical reactions and leads to the high resistance of the cell, as reflected in the respective Nyquist plots. Therefore, these results could underline how the interplay of anionic {V_{10}} with the charge-balancing cation can significantly affect the electrochemical performance of {V_{10}}-based electrode materials.

Electrochemical characterization of Gdm{V_{10}} in lithium-ion battery half-cell and full-cell configurations

Considering the better performance of Gdm{V_{10}} in SIB half-cell, its electrochemical performance as LIB anode material was also tested. For assembling the LIB half-cell, a carbonate electrolyte was used considering its compatibility with the Li metal counter electrode as shown in the literature. Although the Gdm{V_{10}} is slightly soluble in carbonate electrolytes (possibly due to the

high polarity of carbonate electrolytes), the extent of solubility is found to be much less compared to Tba{V_{10}} (Figure S8a). In the CV profiles of the LIB half-cell, the redox features and a higher current response in the low voltage region (1.5 to 0.05 V vs. Li^+/Li, Figure 5a) suggests the compatibility of Gdm{V_{10}} as an anode material for LIB. The discharge and charge capacity obtained in the 1st cycles (at 0.05 A g^{-1}) are 856 and 202 mAh g^{-1}, corresponding to a CE of 23% (Figure S8b). The reversible capacity of the cell becomes stable in the following cycles, delivering specific capacity values of 317, 270, 211, 167, and 130 mAh g^{-1} at 0.05, 0.10, 0.25, 0.50, and 1.0 A g^{-1} current densities (Figure 5b). The cycling stability data of the LIB cell (at 0.25 A g^{-1}) shows a gradual increase in capacity to 445 and 550 mAh g^{-1} after 100 and 200 cycles, respectively, and the cell delivers a maximum capacity of 660 mAh g^{-1} after 450 cycles (Figure 5c).

Finally, the performance of the Gdm{V_{10}} anode was investigated in a LIB full cell using $LiFePO_4$ cathode. Before assembling the full cell, pre-cycling the Gdm{V_{10}} electrode in a half-cell configuration was necessary to offset the irreversible capacity loss in the initial discharge. The Gdm{V_{10}}||$LiFePO_4$ cell was cycled in the 1.0 to 3.5 V voltage range. The cell exhibits a sloped GCD profile (Figure 5d), delivering a reversible capacity of 132 mAh g^{-1} at a 0.016 A $g^{-1}_{cathode}$ current density (considering the cathode loading). The cycling stability of the cell at the same current density shows 68% retention of the initial capacity over 50 cycles (Figure 5e). Although the cycling stability of the full-cell is inferior to the state-of-the-art systems, the performance can be further improved by optimizing the pre-lithiation conditions, tuning the particle size of Gdm{V_{10}} material, etc.

Conclusions

This work reports a hydrogen bond strategy to mitigate the solubility of the $[V_{10}O_{28}]^{6-}$ ({V_{10}}) cluster in liquid organic electrolytes targeting its application as electrode material for sodium and lithium-ion batteries. The {V_{10}} cluster stabilized with organic Gdm^+ counterion (Gdm{V_{10}}) was remarkably insoluble in various organic polar solvents, unlike the soluble nature of another {V_{10}} cluster bearing Tba^+ cation (Tba{V_{10}}).

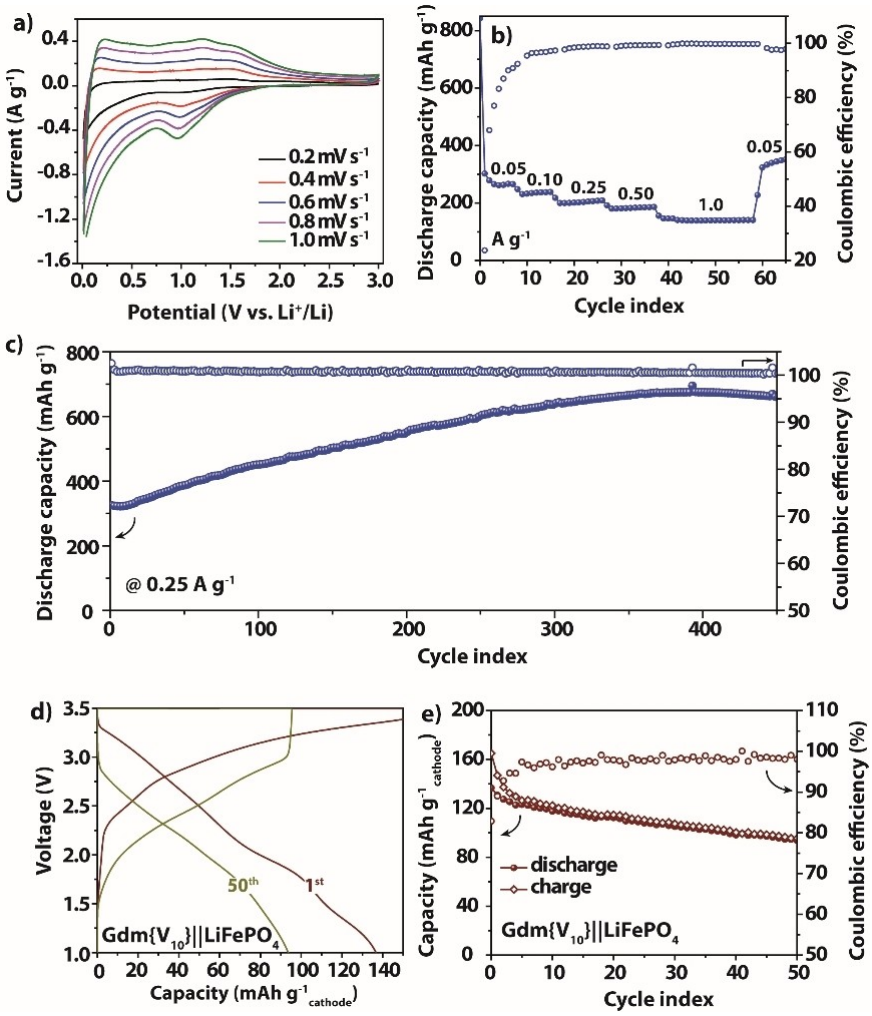

Figure 5. (a) CV profiles recorded at various scan rates, (b) rate capability, and (c) cycling stability performance of the Li||Gdm{V_{10}}; (d) charge-discharge profiles and (e) cycling stability data at 0.016 A $g^{-1}_{cathode}$ of the Gdm{V_{10}}||$LiFePO_4$ full cell assembled with the pre-cycled anode.

The poor solubility of Gdm{V_{10}} is attributed to the hydrogen bonding network among the amino groups in the Gdm^+ ion and {V_{10}} cluster, providing additional ion-pair strength apart from the apparent electrostatic interaction. Benefiting from this feature, applying Gdm{V_{10}} as the anode material in SIB half cells resulted in good rate performance and cycling stability over 150 cycles and 500 cycles at 0.02 and 0.1 $A g^{-1}$, respectively. In contrast, the Tba{V_{10}} electrode experienced rapid capacity fading and retains only 60 $mAh g^{-1}$ capacity within 100 cycles. The electrochemical performance of Gdm{V_{10}} as the anode material in SIB half cells indicates better rate performance and cycling stability than that of the Tba{V_{10}} compound. Finally, the performance of Gdm{V_{10}} as anode material in LIB half-cell and full-cell configurations was also investigated. This study demonstrating cation-assisted stabilization of {V_{10}} for improving its performance as electrode materials will also be beneficial in designing other polyoxometalates-based electrode materials.

Experimental Section

Synthesis of Gdm{V_{10}} and Tba{V_{10}}

In a typical process, 4 g (22 mmol, 1 eq.) of V_2O_5 was dispersed in 30 ml of Mili-Q water, followed by adding an aqueous solution of 6 M NaOH to adjust the pH to 12.5, resulting in the complete dissolution of V_2O_5. The mixture was filtered to remove any undissolved particles or impurities, and the transparent clear solution was heated at 50 °C for 1 h. After cooling to room temperature, the solution was acidified with 4 M aqueous HCl acid until the pH value reached 4.5 (labelled solution A). In a separate beaker, 2.6 g (27.6 mmol, 1.2 eq.) of guanidinium (Gdm^+) chloride salt was dissolved in 50 ml water and dropwise added to solution A under constant magnetic stirring. The obtained bright-orange colored precipitate was filtered and washed thoroughly with water, ethanol, and diethyl ether. Finally, the sample was air-dried for 3 h and vacuum dried at 40 °C for 12 h.

To synthesize Tba{V_{10}}, 8.9 g of (27.6 mmol, 1.2 eq.) tetrabutylammonium (Tba^+) bromide salt was dissolved in 50 ml of water and added dropwise to solution A under magnetic stirring. During the addition of Tba^+ solution, the pH of solution A was maintained at 4.5 using 4 M HCl. The obtained product was washed and dried under the same conditions as for Gdm{V_{10}}.

The solubility of the synthesized materials was qualitatively tested in the ether and carbonate solvent-based electrolytes used for electrochemical characterization. 5 mg of each material was added to 2 ml of electrolyte and the solubility of the material is confirmed from the color change of the solution.

Structural characterization

Single crystal X-ray diffraction (SC-XRD) was performed on a Bruker D8 Quest single-crystal diffractometer with a Photon II detector using Mo Kα radiation (λ = 0.71 Å). The single crystals of Gdm{V_{10}} suitable for SC-XRD were obtained by dissolving the powder in hot water (at 60–65 °C) followed by diffusion of ethanol into the reaction mixture, producing orange needle-shaped long crystals. Powder XRD data of the samples were recorded with STOE Stadi P diffractometer with Mo Kα. ATR-FT-IR spectra were recorded on a PerkinElmer Spectrometer. Raman analysis was carried out with the RENISHAW instrument. Thermogravimetric analysis (TGA) was performed using a NETZSCH TG 209F1 analyzer at a heating rate of 10 $K min^{-1}$ under an air atmosphere.

Electrochemical characterization

For electrode preparation, the active material (Gdm{V_{10}} or Tba{V_{10}}), carbon black, and poly (vinylidene difluoride) (PVDF) binder with a weight ratio of 65:25:10 were homogeneously blended in N-methyl-2-pyrrolidine (NMP) using a planetary mixture. The slurry was coated on a copper foil by the doctor-blade technique. The coated foil was subsequently dried overnight at 80 °C under vacuum for solvent evaporation and punched into electrode discs of 12 mm diameter. The electrodes were further dried at 120 °C for 12 h under vacuum and directly transferred into the argon-filled glovebox ($H_2O < 0.1$ ppm, $O_2 < 0.1$ ppm). The electrodes of 1–2 mg mass loading were used as working electrodes in the half-cell configuration for SIB (sodium metal counter electrode) and LIB (lithium metal counter electrode). An electrolyte made of 1 M $NaPF_6$ dissolved in tetraethylene glycol dimethyl ether (tetraglyme) was used for SIB cells. The cycling voltammetry (CV), galvanostatic charge-discharge (GCD), and electrochemical impedance spectroscopy experiments were carried out using the Bio-Logic BCS 805 instrument. The specific capacity values were normalized with the loading of active material on the working electrode in the half-cell configuration. The Coulombic efficiency (%) in half-cell configuration was calculated from the charge capacity to discharge capacity ratio. For the LIB full cell, the cathode was prepared using commercial $LiFePO_4$ as active material with carbon black additive and PVDF binder (weight ratio 90:5:5). The current rate and capacity values in the full-cell are normalized with respect to the active material loading on the cathode. The Coulombic efficiency (%) in full-cell configuration was calculated from the discharge capacity to charge capacity ratio.

CCDC

Deposition Number(s) 2259868 (Gdm{V_{10}}) contain(s) the supplementary crystallographic data for this paper. These data are provided free of charge by the joint Cambridge Crystallographic Data Centre and Fachinformationszentrum Karlsruhe Access Structures service.

Author Contributions

Meena Ghosh: Conceptualization, development of the methodology, validation, formal analysis, writing – the original draft (lead), data curation, writing – review & editing, investigation, and visualization; Dieter Sorsche: Resources, formal analysis, and writing – review & editing; Rezwana Binte Ahmed: Resources; Montaha Anjass: Conceptualization, resources, writing – the original draft (supporting), writing – review & editing, supervision, project administration, funding acquisition. All authors have approved the final version of the article.

Acknowledgements

This work contributes to the research performed at CELEST (the Center for Electrochemical Energy Storage Ulm-Karlsruhe) and was funded by the Deutsche Forschungsgemeinschaft (DFG,

German Research Foundation) under Germany's Excellence Strategy – EXC 2154 – Project number 390874152 (POLiS Cluster of Excellence). Financial support by Ulm University, the Helmholtz-Gemeinschaft (HGF) is gratefully acknowledged. M. A. acknowledges the State of Baden-Württemberg for a Margarete-von-Wrangell fellowship and the Baden Württemberg Stiftung (Elite programme for Postdocs). Open Access funding enabled and organized by Projekt DEAL.

Conflict of Interests

There are no conflicts to declare.

Data Availability Statement

The data that support the findings of this study are available from the corresponding author upon reasonable request.

Keywords: electrode material · ion-pair interaction · organic countercation · polyoxovanadate · solid-state stabilization

[1] a) Y. Zhang, J. Liu, S.-L. Li, Z.-M. Su, Y.-Q. Lan, *EnergyChem.* **2019**, *1*, 100021; b) H. D. Pratt III, N. S. Hudak, X. Fang, T. M. Anderson, *J. Power Sources.* **2013**, *236*, 259.
[2] H. Miras, D.-L. Long, L. Cronin, *in Adv. Inorg. Chem. vol. 69*, Elsevier. **2017**, pp. 251–286.
[3] M. Anjass, G. A. Lowe, C. Streb, *Angew. Chem. Int. Ed.* **2021**, *60*, 7522.
[4] a) S. Hartung, N. Bucher, H.-Y. Chen, R. Al-Oweini, S. Sreejith, P. Borah, Z. Yanli, U. Kortz, U. Stimming, H. E. Hoster, *J. Power Sources.* **2015**, *288*, 270; b) H.-Y. Chen, J. Friedl, C.-J. Pan, A. Haider, R. Al-Oweini, Y. L. Cheah, M.-H. Lin, U. Kortz, B.-J. Hwang, M. Srinivasan, *Phys. Chem. Chem. Phys.* **2017**, *19*, 3358; c) S. Lu, Y. Lv, W. Ma, X. Lei, R. Zhang, H. Liu, X. Liu, *Inorg. Chem. Front.* **2017**, *4*, 2012.
[5] A. Xie, C.-A. Ma, L. Wang, Y. Chu, *Electrochim. Acta.* **2007**, *52*, 2945.
[6] H. Liu, J. Wang, *Ionics* **2010**, *16*, 379.
[7] M. H. Anjass, M. Deisböck, S. Greiner, M. Fichtner, C. Streb, *ChemElectroChem* **2019**, *6*, 398.
[8] S. Greiner, M. H. Anjass, M. Fichtner, C. Streb, *Inorg. Chem. Front.* **2020**, *7*, 134.
[9] a) G. M. Bosch, A. Sarapulova, S. Dsoke, *ChemElectroChem* **2021**, *8*, 656; b) M. Priyadarshini, S. Shanmugan, K. P. Kirubakaran, A. Thomas, M. Prakash, K. Vediappan, *RSC Adv.* **2021**, *11*, 19378.
[10] a) L. Van Gelder, A. Kosswattaarachchi, P. Forrestel, T. Cook, E. Matson, *Chem. Sci.* **2018**, *9*, 1692; b) J. Friedl, M. V. Holland-Cunz, F. Cording, F. L. Pfanschilling, C. Wills, W. McFarlane, B. Schricker, R. Fleck, H. Wolfschmidt, U. Stimming, *Energy Environ. Sci.* **2018**, *11*, 3010.
[11] a) F. Leroy, P. Miró, J. M. Poblet, C. Bo, J. Bonet Ávalos, *J. Phys. Chem.* B **2008**, *112*, 8591; b) A. Misra, K. Kozma, C. Streb, M. Nyman, *Angew. Chem. Int. Ed.* **2020**, *59*, 596.
[12] P. Mason, G. Neilson, C. Dempsey, A. Barnes, J. Cruickshank, *Proc. Nat. Acad. Sci.* **2003**, *100*, 4557.
[13] X. Wang, H.-X. Liu, X.-X. Xu, X.-Z. You, *Polyhedron* **1993**, *12*, 77.
[14] S. Nakamura, T. Ozeki, *J. Chem. Soc. Dalton Trans.* **2001**, 472.
[15] a) R. A. Frenzel, G. P. Romanelli, L. R. Pizzio, *J. Mol. Catal.* **2018**, *457*, 8; b) J. Díaz, L. R. Pizzio, G. Pecchi, C. H. Campos, L. Azócar, R. Briones, R. Romero, A. Henríquez, E. M. Gaigneaux, D. J. C. Contreras, *Catalysts.* **2022**, *12*, 507.
[16] R. Meenakshi, K. Shakeela, S. Kutti Rani, G. Ranga Rao, *Catal. Lett.* **2018**, *148*, 246.
[17] I. Omri, T. Mhiri, M. Graia, *J. Mol. Struct.* **2015**, *1098*, 324.
[18] C. Cao, K. Wu, W. Yuan, Y. Zhang, H. Wang, *Polym. Fibers.* **2017**, *18*, 1040.
[19] E. Hryha, E. Rutqvist, L. Nyborg, *Surf. Interface Anal.* **2012**, *44*, 1022.
[20] H. Wang, Y. Xiao, C. Sun, C. Lai, X. Ai, *RSC Adv.* **2015**, *5*, 106519.
[21] a) X. Wang, L. Qi, H. Wang, *Ionics* **2020**, *26*, 4533; b) H. He, D. Sun, Y. Tang, H. Wang, M. Shao, *Energy Storage Mat.* **2019**, *23*, 233.
[22] a) J. Hwang, K. Takeuchi, K. Matsumoto, R. Hagiwara, *J. Mater. Chem. A.* **2019**, *7*, 27057; b) Y. Zhao, T. Zhou, T. Ashirov, M. E. Kazzi, C. Cancellieri, L. P. Jeurgens, J. W. Choi, A. Coskun, *Nat. Commun.* **2022**, *13*, 2575.
[23] C. Wang, J. Yan, T. Li, Z. Lv, X. Hou, Y. Tang, H. Zhang, Q. Zheng, X. Li, *Angew. Chem. Int. Ed.* **2021**, *133*, 25217.

Manuscript received: May 1, 2023
Revised manuscript received: August 15, 2023
Accepted manuscript online: August 24, 2023
Version of record online: October 5, 2023